DOI: 10.13009/EUCASS2025-301
11TH EUROPEAN CONFERENCE FOR AERONAUTICS AND SPACE SCIENCES (EUCASS)

Experimental Investigation of Electroaerodynamic Propulsion: Velocity-Information-Based Thrust and Self-Induced Drag Estimation

Dominic POEPPE†*, Alina KUHN, Ferdinand ELSNER, and Jochen KRIEGSEIS*

Institute of Fluid Mechanics (ISTM), Karlsruhe Institute of Technology (KIT)
Karlsruhe, Germany

poeppe@kit.edu · kriegseis@kit.edu
† Corresponding author

Abstract

An electroaerodynamic thruster in wire-to-droplet airfoil configuration is investigated experimentally by means of particle image velocimetry in combination with a load cell and electrical characterization. While the time-averaged velocity fields appear smooth and show consistent topology across a large voltage regime, instantaneous velocity fields reveal wake instabilities. The potential of estimating thrust based on velocity information is showcased, where different approaches are contrasted. The results show good agreement with direct load cell measurements. Finally, options and challenges for the estimation of self-induced drag are discussed.

1. Introduction

Ionic wind, also known as electroaerodynamic (EAD) propulsion, has the potential to be a reasonable alternative to traditional propulsion methods relying on moving parts in specific applications. The solid-state nature of EAD thrusters inherently provides several potential benefits, such as near-silent operation, zero combustion emissions, and reduced maintenance requirements. The field has seen renewed interest in recent years with studies on electrode shape, thruster array scaling, environmental effects, and a successful demonstration of meter-scale EAD-propelled aircraft, to name a few.[1,2,8,11,18,22,23,26]

The operating principle of positive corona discharge EAD thrusters is based on imparting momentum onto neutral air molecules by collisions with ions, which are in turn accelerated by the electric drift field in the so-called drift region between two electrodes. The sharply curved emitting electrode, called emitter, has positive potential, while the collecting electrode, called collector, is grounded. The electric field strength reaches its peak in the immediate vicinity around the emitter, leading to an ionization cascade. The upper limit of thrust T can be approximated analytically when neglecting space charge effects as $T = Id/\mu$, where I is the discharge current, d is the gap distance between the emitter and collector electrodes, and μ is the ion mobility.[15,25] Thrust of practical single thrusters is furthermore, but not exhaustively, a function of emitter and collector shape influencing the electric field shape and body drag, air speed, environmental quantities, and three-dimensional effects due to finite span.

Key metrics of EAD thrusters include absolute thrust (or thrust density) and efficiency (thrust per power), which exhibit an inverse relationship. Optimizing the Pareto front of these two quantities is thus key to future high-performance thruster design. Measuring the thrust of an EAD thruster can be done in various ways. Arguably, the most straightforward is using load cells; however, their feasibility can be limited depending on the specifics of the experimental setup. For instance, due to grounded measurement devices, parasitic electric fields can directly affect the primary discharge. As an alternative, discharge-based thrust production can be estimated from velocity information using integral and differential methods. Previous investigations into these methods include Kriegseis et al.,[13] Monrolin et al.,[17] and Belan et al.[2]

The present study improves on existing investigations by extending the velocity domain to near-wall information, thus enabling quantification of the momentum transfer contributors in the direct collector vicinity. Gaining insight into this self-induced drag is crucial for electrode geometry optimization and builds on similar methodology and experience with dielectric barrier discharge.

DOI: 10.13009/EUCASS2025-301

2. Parameter Decomposition

The parameter space of ionic thrusters is primarily dictated by the transfer function of input to output quantities. Parameterized environment and setup quantities further influence this transfer function, which makes the following parameter classification a feasible way to group influencial factors:

- control quantities (input)
- resulting transfer quantities (output)
- environmental quantities (boundary condition)
- materials & geometries

While the impact of environmental influences, and geometry and material choices becomes of utmost importance upon truster application, it appears likewise crucial to first clarify the primary transfer function of the control effort prior to the investigation of such influences. This paper accordingly aims to improve the understanding of the transfer function without varying the latter groups' parameters. Nonetheless, an overview is given below to acknowledge the influence of all parameter groups and to concisely define the reference configuration.

2.1 Control Quantities (Input)

Operating Voltage V The operating voltage is the major control quantity for corona discharge. Any control effort will largely revolve around the precise adjustment of this quantity.

2.2 Resulting Transfer Quantities (Output)

Thrust Production T One of the key metrics of thruster optimization, especially thrust per power and thrust density.

Ionic Current I The generated current resulting from the discharge serves as a valuable measure for the discharge intensity and identification of the discharge regime.

Power Consumption P In terms of efficient energy usage for the produced thrust, the overall power consumption serves as reference in the denominator of any electric to fluid-mechanic efficiency evaluation approach.

Velocity Field $u(x, y)$ Availability of velocity field in the vicinity and around the thruster device provides valuable insight into the footprint of the propulsion effort on the surrounding fluid. Beyond the explicit knowledge of a measured thrust, the resulting velocity fields also provide the basis of further evaluation options regarding implicit thrust estimation approaches.

2.3 Environmental Quantities (Boundary Condition)

Air Speed U_∞ The kinematic impact of the environment has been shown to have a significant influence on the effective momentum transfer, since the drift velocity of the charges no longer acts upon a quiescent environment.[7,22] Moreover, the momentum transfer leads to diminished effective thrust production.

Relative Humidity RH An increase in air humidity decreases the effective thrust of ionic thrusters at constant voltage due to decreased ion mobility.[25,27] In ground tests, this environmental quantity has the single largest impact on thruster performance.

Pressure p The breakdown voltage of gases follows Paschen's law, which in the present case of a fixed and sufficiently large geometry limits the operating voltage at lower pressures while simultaneously increasing current due to increased ion mobility. In combination with reduced momentum transfer due to lower air density, this leads to reduced performance and efficiency.[12,25]

Temperature T Temperature presumably only has a minor impact on corona discharge characteristics at ground level. Nonetheless, for comparability and repeatability, it is crucial to record this quantity.

DOI: 10.13009/EUCASS2025-301

2.4 Materials & Geometries

Emitter Diameter d_e The emitter diameter follows the compromise between a quasi-non-intrusive ion source and a robust structure. Furthermore, smaller diameters lead to higher local electric fields, thus enhancing the discharge character of the thruster device.

Collector Shape While fundamental research also investigated cylinders as collector geometry, droplet-shaped airfoils and the NACA00xx series appear promising slender bodies for good aerodynamic properties (friction and form drag) for practical applications of EAD thrusters.

Thickness t **and Chord** c Thickness and chord, often expressed as the thickness-to-chord ratio t/c, must be chosen carefully as the thickness especially plays an important role in shaping the electric field in the proximity of the collector, and both thickness and chord directly affect pressure and friction drag. Notably, wake properties of slender aerodynamic bodies improve with increasing chord while the friction-drag inducing surface area increases.

Span b This quantity is subject to scaling efforts for practical applications as losses due to edge effects diminish with increasing span. For the present study, the flow at mid-span is considered two-dimensional due to the distance from the edges and symmetry considerations.

Inter-Electrode Gap Distance d The distance d between emitter and collector scales the strength of the attainable electric field. Consequently, this quantity is usually determined in combination with the chosen operating voltage to achieve a strong discharge while remaining below the critical dielectric breakdown voltage.

3. Experimental Setup

The experimental setup for the quiescent-air investigation consists of a single wire-to-airfoil pair, which can be seen in Figure 1. While arrays of emitter-collector pairs have been shown to be superior,[3,8,15–18,22,23] this deliberate choice is made in order to facilitate optimum optical access and to build an undisturbed baseline measure of a single pair.

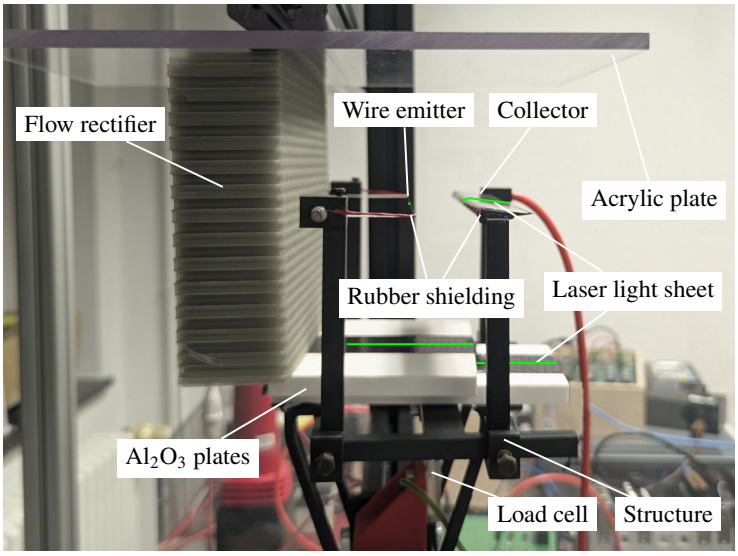

Figure 1: Experimental setup of the thruster used with all major components labeled. Perspective similar to PIV camera.

DOI: 10.13009/EUCASS2025-301

The geometric and operating parameters for the present work are summarized as follows, with additional parameters for Section 4 in parentheses:

- Span $b = 200\,\text{mm}$
- Inter-electrode gap distance $d = 30\,\text{mm}$, ($d = 20\,\text{mm}$)
- Wire emitter with diameter of $D_e = 100\,\mu\text{m}$
- Droplet airfoil collector
  - Thickness to chord ratio $t/c = 0.24$
  - Thickness $t = 6\,\text{mm}$
- operating voltage 15 kV to 30 kV, (0 kV to 30 kV)

The layout of the spatial arrangement and the corresponding dimensions are furthermore sketched in Figure 2.

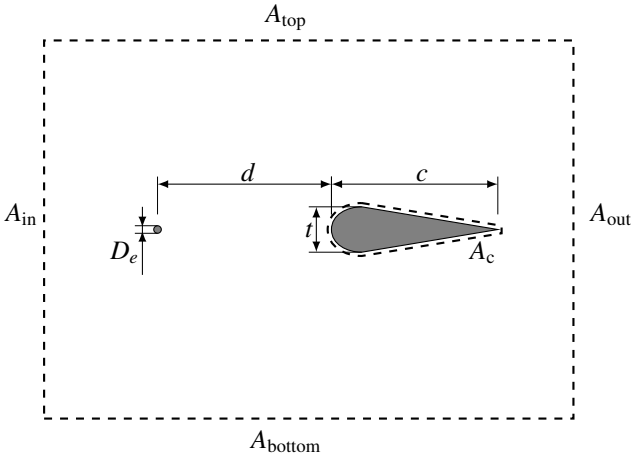

Figure 2: Geometric parameters of the wire-to-airfoil thruster used in this paper. Surrounding the thruster is the control volume definition used in the integral momentum balance in a later chapter. Not to scale.

The emitter wire is a constantan alloy, while the collector is a stereolithography 3D-printed structure, coated with aluminum and polished to reduce undesirable diffuse laser light reflection. The span-wise edges of the emitter and collector are coated in an insulating rubber to eliminate edge effects such as reverse corona discharge and arc discharge. Emitter and collector are affixed to an insulating plastic structure, which is mounted to the load cell. To reduce the strength of the parasitic electric field between the emitter and the grounded load-cell, Al_2O_3 plates are installed due to their high permittivity. The operating voltage is provided by a GBS Elektronik Minipuls 6 in combination with a high-voltage multiplier cascade and regulated using a PID controller.

In order to reduce the effects of fluctuating inflow conditions arising from potential large-scale motions within the enclosure, a honeycomb structure acts as a flow rectifier for the data presented in Section 4 and Section 5. It is positioned 60 mm upstream of the emitter. Since this rectifier introduces aerodynamic drag and would thus need to be accounted for in the momentum balance calculation of Section 6, it is instead omitted for the velocity-information-based thrust estimation. An acrylic plate is installed above the thruster to mirror the boundary conditions of the Al_2O_3 plate below the thruster.

For the resulting transfer quantities, the total thrust is measured using a 5 N bending beam load cell while the current is measured between the collector and ground, thus only the corona current is measured, omitting stray currents. The current measurement makes use of a galvanically isolated circuit to prevent measurement instrumentation damage due to overcurrent. The state variables – i.e., relative humidity, pressure, and temperature – were additionally recorded for monitoring purposes only and are listed in the appendix for all data in the following sections.

In order to quantify the velocity field using PIV, laser light from a Quantel EverGreen Nd:YAG laser (Wavelength 532 nm) is directed through an articulated mirror arm and cylindrical optics to illuminate the plane of symmetry at mid-span of the emitter-collector pair. Due to the shadow cast by the collector, the region below it is invisible to the PIV. A pco.edge 5.5 sCMOS camera (resolution of 2560 x 2160 pixels, bit depth 16 bit) is installed slightly above the span-wise axis to reduce obstructions. This perspective distortion is corrected using a calibration target. The resulting scaling is $\sim 26\,\text{pixel}\,\text{mm}^{-1}$ and double images are captured at a rate of 10 Hz and a pulse delay of 100 µs. The flow field is seeded with incense particles as these are generally regarded to be unaffected by the electric field.[9,17] An enclosure of $1\,\text{m} \times 1\,\text{m} \times 1.5\,\text{m}$ enables homogeneous tracer density.

Due to diffuse light reflection and thus low signal-to-noise ratio in the vicinity of the collector, image preprocessing is performed. Average images are calculated and subtracted from the instantaneous images. Furthermore, the images are high-pass filtered with a 7 pixel kernel. The collector and accompanying shadow are masked. Multi-grid interrogation is used with an initial / final window size of 64 pixel / 8 pixel and an overlap of 50 %. For outlier detection, a normalized median test[24] with a threshold of 3.0, a maximum displacement test of 17 pixel, and a maximum displacement difference of 2 pixel are used. Outliers are replaced using lower-order peaks and interpolation.

4. Discharge Characteristics

In a preliminary step, the discharge characteristics of the setup are evaluated. By comparison with analytical, numerical, and experimental work, this serves to verify the electromechanical setup and the data acquisition. Various dimensional

DOI: 10.13009/EUCASS2025-301

parameters are discussed at a gap distance of 20 mm and 30 mm and voltage from 0 kV to breakdown. Figure 3a shows the relationship of power per meter P/b to voltage V. At space-charge-limited conditions, zero air speed, and a sufficient distance from the ignition voltage V_i, the current density follows a quadratic fit as described by the Mott-Gurney law.[6] Thus, the power follows a cubic fit, plotted in Figure 3a. Thrust density is expected to scale quadratically with voltage, as predicted by Cooperman,[4] which agrees reasonably well with the experimental data presented in Figure 3b as thrust per meter T/b against $V(V - V_i)$, where V is the operating voltage and V_i the ignition voltage.

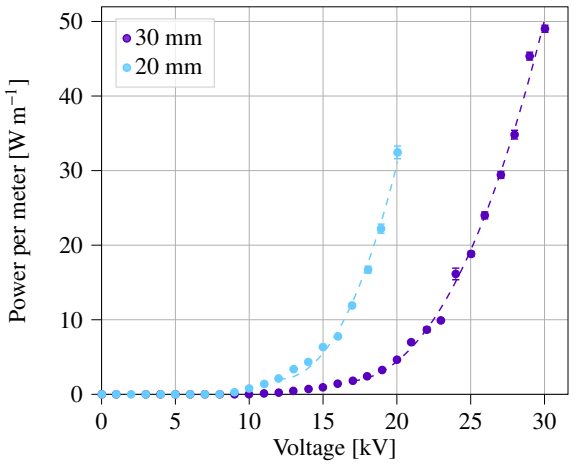

(a) Cubic relationship of power per meter vs. voltage.

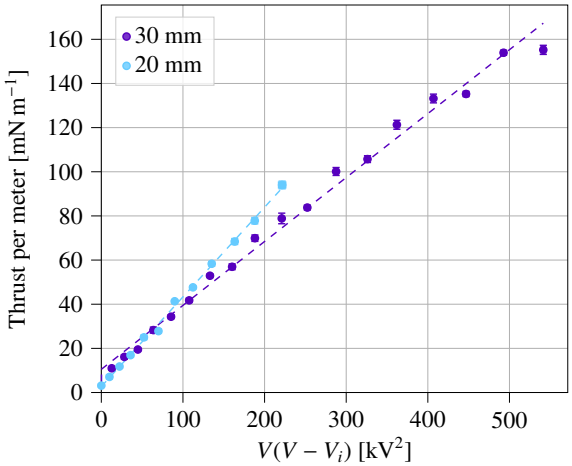

(b) Linear relationship of thrust per meter vs. $V(V - V_i)$, V is the operating voltage and V_i the ignition voltage.

Figure 3: Discharge characteristics at two gap distances d = 20 mm and 30 mm.

Figure 4a illustrates the relationship between the generated thrust per meter and the required power per meter. The curve for both gap distances shows a diminishing gradient up to the breakdown voltage. This behavior highlights a fundamental limitation in EAD thruster design, where achieving higher thrust necessitates a disproportionate increase in power consumption, thereby reducing the overall efficiency. This inverse relationship between thrust and efficiency is explicitly confirmed in Figure 4b. For both the 20 mm and 30 mm gap configurations, a clear trend of decreasing efficiency with increasing voltage is observed. This experimental result aligns well with the simplified analytical model, which combines the thrust approximation $T = Id/\mu$ from Section 1 with the electrical power formula $P = IV$ to yield an efficiency relationship of $T/P \propto d/(V\mu)$. Both the inverse proportionality of the voltage V and the direct proportionality of the gap distance d is supported by the data in Figure 4b.

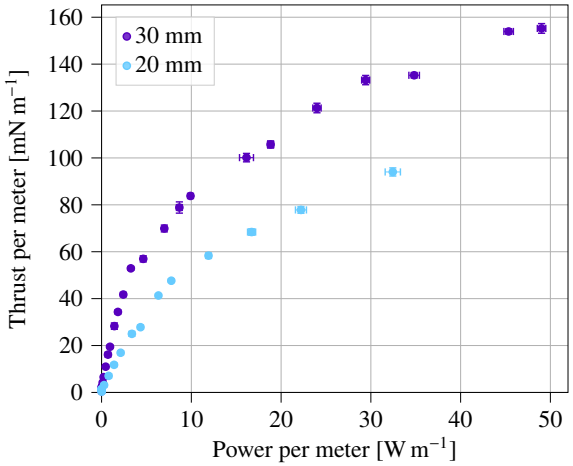

(a) thrust per meter vs power per meter

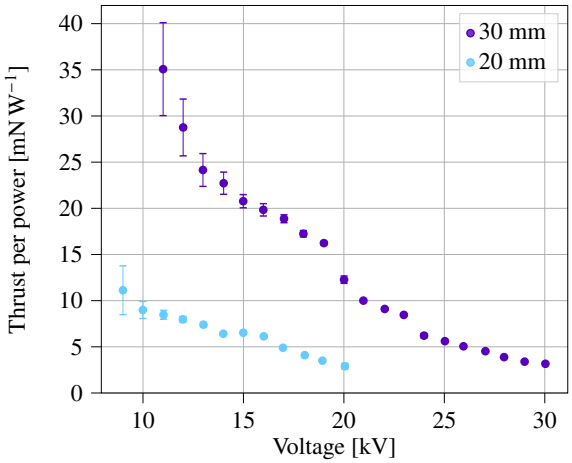

(b) Thrust per power vs voltage

Figure 4: Discharge characteristics at two gap distances d = 20 mm and 30 mm.

DOI: 10.13009/EUCASS2025-301

5. Velocity Fields

5.1 Time-Averaged Velocity Fields

Figure 5 shows the time-averaged velocity fields for operating voltages of 20 kV and 30 kV, calculated from 500 instantaneous velocity fields. The emitter and collector are drawn in gray. The collector casts a shadow in the otherwise laser-illuminated region, which is visible as the black region.

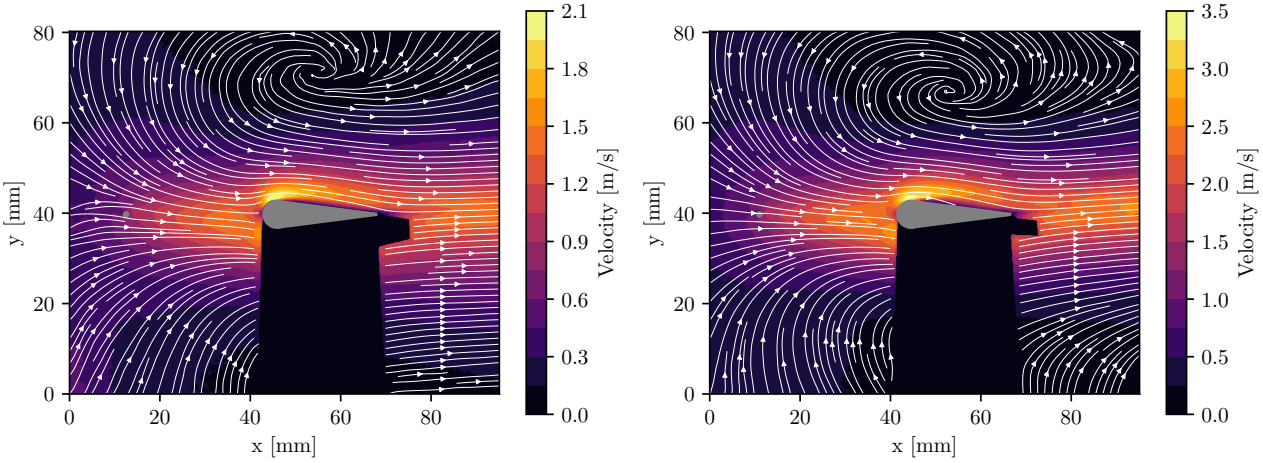

(a) 20 kV (b) 30 kV

Figure 5: Time-averaged velocity fields at different operating voltages V and constant gap distance $d = 30$ mm.

Both velocity fields shown are topologically similar, exhibit horizontal symmetry, and show good agreement with numerical data generated by Picella et al.[20] This holds true for all other evaluated velocity fields not shown here. A distinct flow acceleration region due to the body force of the corona discharge momentum transfer can be seen between emitter and collector. A second acceleration region can be observed due to the suction peak of the collector airfoil shape. This leads to the maximum velocity coinciding with the location of maximum thickness.

Prominent vortices can be seen either above or below the thruster, possibly due to the presence of the acrylic and Al_2O_3 plates. However, these vortices only play a minor role in the momentum transfer, since they are entirely at near-zero velocities. Furthermore, the expected array configurations of practical thruster designs will greatly influence the boundary conditions above and below a single emitter-collector pair.

The similarity of the topology of the presented velocity fields enables normalization and averaging across multiple voltages. The velocity fields are normalized using their respective maximum velocities and averaged. Figure 6a shows the maximum velocity of each time-averaged velocity field plotted against the operating voltage. The bars show standard deviation. While a large standard deviation in the maximum velocities is arguably not surprising due to fluctuations in turbulence and electric field, and errors in the PIV measurement, the sudden jump in standard deviation of the voltage and maximum velocity for the 30 kV measurement can be attributed to the onset of streamer formation.

The relationship of maximum velocity to operating voltage displays a clear linear trend, as also shown by, e.g., Robinson.[21] For the present experimental parameters, this results in the following formulation valid from 15 kV to 30 kV:

$$u = (0.141V - 0.722)\hat{u} \tag{1}$$

where u is the physical velocity, V the operating voltage, and $\hat{u}$ the normalized velocity. The corresponding average normalized velocity field can be seen in Figure 6b.

5.2 Instantaneous Velocity Fields

While the time-averaged velocity fields shown in Section 5.1 appear to show a smooth and attached flow topology, the instantaneous velocity fields show a different picture. Figure 7 contrasts two snapshots at 20 kV and 30 kV. While the top row shows a relatively smooth wake topology, the bottom row shows the onset of wake instabilities. Wake vortices in ionic thrusters are known and expected to occur in wire-to-cylinder configurations;[17] however, the present findings

DOI: 10.13009/EUCASS2025-301

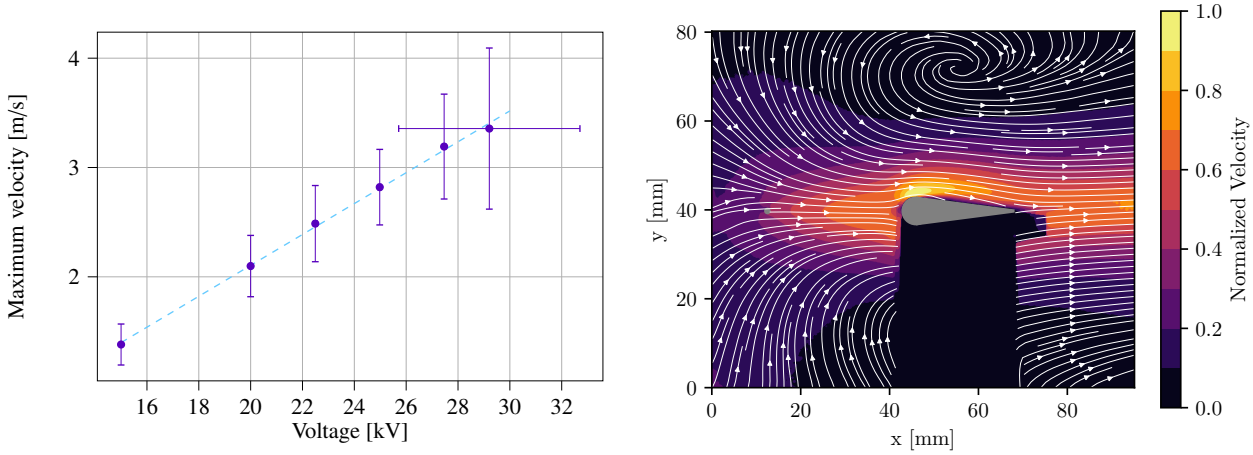

(a) Linear relationship between maximum velocity of the time-averaged velocity field and operating voltage.

(b) Normalized velocity field following the function in Equation (1).

Figure 6: Normalization of six time-averaged velocity fields.

are evidence that this vortex shedding can also occur with droplet airfoils. This insight is of particular importance to designs of multi-stage thruster arrays, since fluctuating inflow conditions at the downstream thrusters could lead to further increased instability and increases in aerodynamic losses.

The vortex formation could be due to an adverse pressure gradient at the suction peak, exacerbated by the non-uniform ionic wind velocity distribution. An alternative explanation can be found in the sensitive behavior to small perturbations of the electric field of a single emitter-collector pair. In our experiments, the footprint of this could be seen in the streamlines of instantaneous velocity fields fluctuating up and down, even with laminar inflowing air. Emitter arrays, while exhibiting other experimental difficulties, have been shown to be less susceptible to these velocity field fluctuations.[1] Of interest could be a comparison of droplet airfoils to symmetric NACA airfoils with less severe adverse pressure gradient.

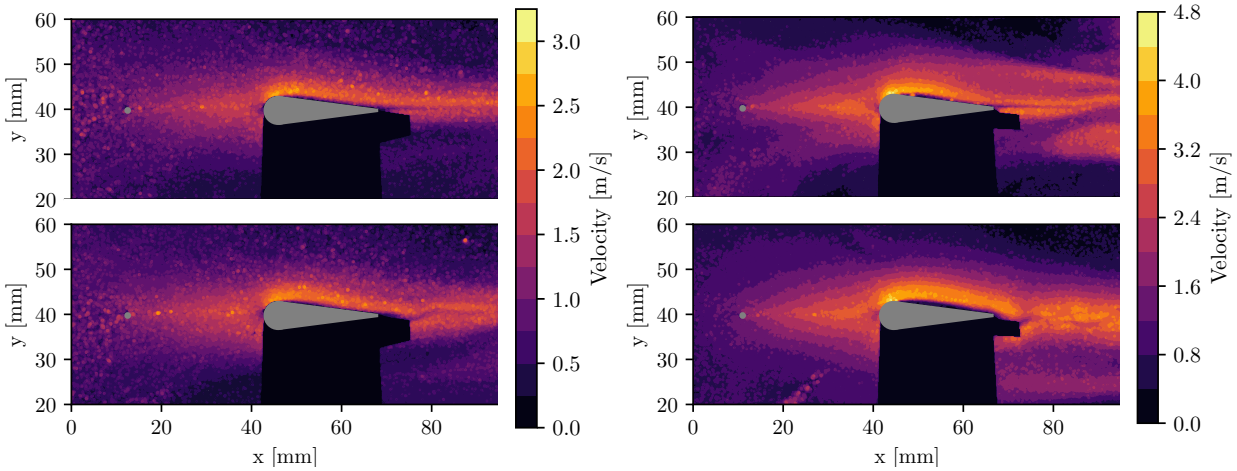

(a) 20kV

(b) 30kV

Figure 7: Instantaneous velocity fields at random time stamps for 20 kV and 30 kV.

6. Velocity-Information-Based Thrust Estimation

As mentioned in Section 3, the upstream rectifier is removed for this section. To assess the impact of this, a convergence analysis is conducted at the highest velocity in the flow field for both configurations (with and without rectifier), but otherwise unchanged setup and a constant operating voltage. Figure 8 shows the coefficient of variation which is

DOI: 10.13009/EUCASS2025-301

defined as σ/μ, with the standard deviation σ and the mean μ, each evaluated for the cumulative set of velocity fields $[1, 500]$. Both configurations converge to a similar level, indicating a similar level of velocity fluctuation. The figure shows the convergence analysis for 25 kV. Other voltages behave similarly.

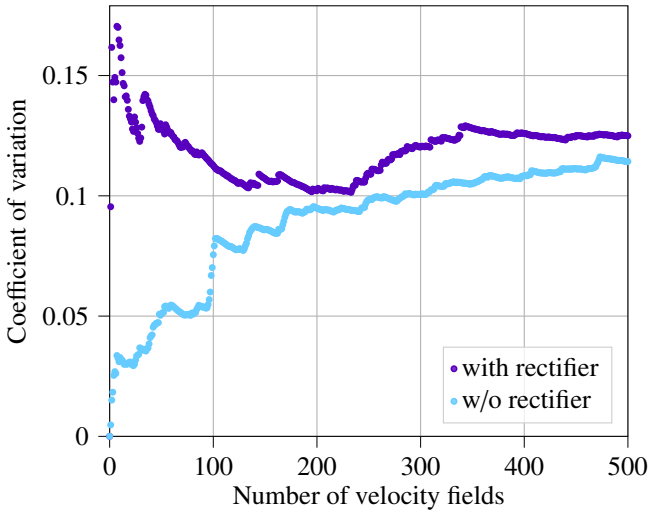

Figure 8: Convergence analysis of the location of maximum velocity for a voltage of 25 kV with and without rectifier. The measurement without rectifier extends to 1000 velocity fields but is cut off for comparability.

Thrust is estimated using the integral momentum balance for a control volume (CV) of volume V and surface area A as defined in Figure 2. The Integral momentum equation is given as:

$$\frac{\mathrm{d}}{\mathrm{d}t}\iiint_V \rho u_j \,\mathrm{d}V + \iint_A \rho u_j u_i n_i \,\mathrm{d}A = -\iint_A p n_j \,\mathrm{d}A + \iint_A \tau_{ij} n_i \,\mathrm{d}A + \iiint_V \rho k_j \,\mathrm{d}V \tag{2}$$

where ρ is the air density, u_j the velocity component in j-direction, n_i the normal vector of the CV boundary in i-direction, p the pressure, τ_{ij} the viscous shear stresses, and k_j are body forces.

For the present case of horizontal thrust, $j = 1$. Furthermore, steady flow is assumed and thus no temporal change of momentum inside the CV. Viscous forces only exist on the top and bottom CV boundaries and on the collector surface A_c. At the top and bottom CV boundaries, they can be neglected at a sufficient distance. The inflowing boundary is positioned far away such that quiescent conditions can be assumed, i.e.,

$$\iint_{A_\mathrm{in}} \rho u_1 u_i n_i \,\mathrm{d}A = 0 \quad \text{and} \quad -\iint_{A_\mathrm{in}} p n_1 \,\mathrm{d}A = p_\infty. \tag{3}$$

The outflowing boundary is positioned a short distance behind the collector, such that pressure has recovered and thus

$$-\iint_{A_\mathrm{out}} p n_j \,\mathrm{d}A = -p_\infty. \tag{4}$$

In the present case, the electroaerodynamic force F_EAD is the only non-negligible body force. Thus,

$$\iiint_V \rho k_1 \,\mathrm{d}V = \iiint_V \rho_q E \,\mathrm{d}V = F_\mathrm{EAD} \tag{5}$$

where ρ_q is the space charge density and E the electric field. Importantly, the electroaerodynamic force F_EAD must not be mistaken with the thrust T measured by the load cell, but rather the thrust T is equal to the electroaerodynamic body force F_EAD minus an unknown self-induced drag[5,14] according to

$$T = F_\mathrm{EAD} - F_d\,, \tag{6}$$

which is comprised of pressure and/or friction drag at emitter, collector, and other surfaces. The self-induced drag force F_d is dominated by the collector due to its size and is thus equal to the integral of the pressure and shear stress acting on the CV boundary A_c:

DOI: 10.13009/EUCASS2025-301

$$-\iint_{A_c} p n_1 \, \mathrm{d}A + \iint_{A_c} \tau_{i1} n_i \, \mathrm{d}A = -F_d \tag{7}$$

whereby the relative contribution of pressure and friction drag to total drag is unknown. Applying Einstein summation convention, this leads to:

$$\iint_{A_{\text{out}}} \rho u_1^2 \, \mathrm{d}A = -F_d + F_{\text{EAD}} = T \, . \tag{8}$$

Or for the 2D case:

$$\int_{-\infty}^{\infty} \rho u_1^2 \, \mathrm{d}y = \frac{T}{b} \tag{9}$$

where b is the span. Note that the integration bound of infinity is only valid for the quiescent case. The formulation according to Equation (9) is similar to the one made by Hoskinson et al.[10] for use with DBD actuators in quiescent conditions.

Two notable investigations are presented in contrast to this approach. First, Belan et al.[2] used pitot measurements in an enclosed setup with a screen to reduce turbulence of the inflowing air. They positioned the inflowing boundary much closer to the thruster and did not neglect pressure p at the inflowing boundary and instead calculated the pressure losses due to the screen using Bernoulli's theorem.

Secondly, Monrolin et al.[17] do not neglect the inflowing momentum but do assume ambient pressure on all boundaries. By adding contributions of momentum fluctuations, they find a good agreement with their digital scale measurements.

Similarly, we also find that fluctuations in momentum flux need to be taken into account. We achieve this by evaluating Equation (9) for each instantaneous velocity field and time-averaging the thrust. As can be seen in Figure 9, calculating the outflowing momentum flux from the average velocity field, thus discarding fluctuation contributions, leads to underestimating the thrust produced. By including fluctuation contributions, the agreement with the load cell measurement is much improved. The figure also makes apparent a drawback of estimating thrust from velocity data, which is the much larger standard deviation compared to the load cell measurements.

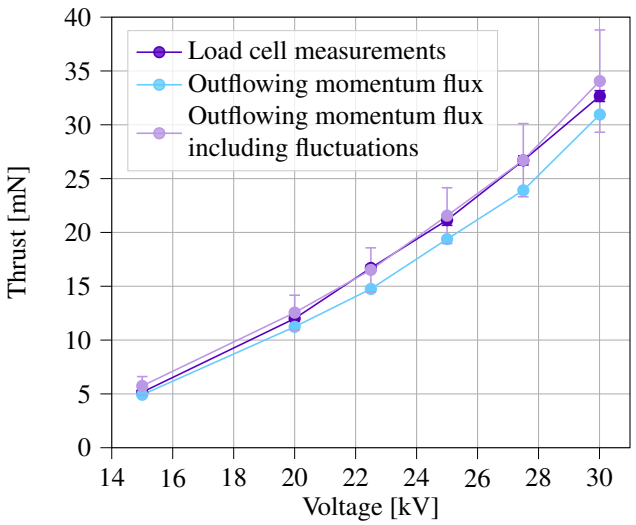

Figure 9: Two different methods of computing thrust from the momentum flux of measured velocity fields in comparison to direct load cell measurements.

This becomes even more apparent when looking at the time-resolved data of outflowing momentum flux and load cell measurement in Figure 10. Even with filtering, the signal still exhibits large fluctuations. Either these fluctuations are physically present and are damped through the electroaerodynamic interaction between gas and solid, or the fluctuations are due to evaluation error of instantaneous PIV fields.

DOI: 10.13009/EUCASS2025-301

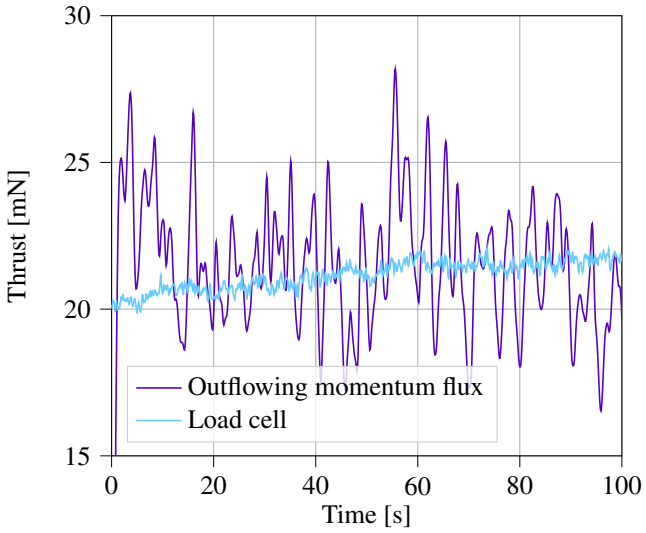

Figure 10: Time-resolved data of outflowing momentum flux and load cell measurement at 25 kV. Both values are third-order Butterworth filtered. Cutoff frequency for outflowing momentum flux: 0.5 Hz. Cutoff frequency for load cell: 2 Hz.

7. Drag Estimation

The distinction between thrust T and electroaerodynamic force F_{EAD} in Equation (6) underlines the need to optimize two parameters to increase thrust density and efficiency: increasing F_{EAD} and decreasing F_d. For a comprehensive evaluation metric across different thruster configurations, it is therefore important to quantify the drag force. Through numerical estimation, it is concluded that friction drag is the dominating contributor to the total drag force F_d, therefore, a first attempt focuses on estimating friction drag for the data presented in Section 5.

For the case of reliable near-wall velocity data, the estimation of friction drag is relatively straightforward. The velocity gradient normal to the wall is evaluated at the wall, i.e.,

$$\tau_w = \mu \left.\frac{\partial u}{\partial y}\right|_{\mathrm{wall}} \tag{10}$$

where τ_w is the wall shear stress, u is the wall-parallel velocity component, and y is the wall-normal direction. Integrating the wall shear stress τ_w over the area of the wall results in the total friction drag force. PIV measurements are often not highly resolved enough to capture the velocity information immediately above the wall, and in the present case, the collector surface introduces light pollution and thus measurement uncertainty. Furthermore, for the present study, the location of the wall is only estimated. To overcome this information deficiency, the available boundary layer velocity information is typically fitted with mathematical descriptions of standard boundary layers in order to extrapolate the profile to the wall and calculate the velocity gradient.

The boundary layer forming on the collector surface is examined at several streamwise positions. For this purpose, the velocity field is linearly interpolated along the normal of the surface. An example of the resulting velocity field can be found in Fig. 11. As discussed in Section 5.2, the time-averaged flow field is constructed of strongly fluctuating instantaneous field data. The attempt of a fit according to Nickels[19] is made, but the characteristic features of a turbulent boundary layer, such as logarithmic layer, are not recognizable. It is concluded that the resulting velocity profile is not a turbulent boundary layer in the classical sense. The boundary layer has presumably detached from the wall in parts, either due to inappropriate inflow or due to the pressure gradient imposed on the boundary layer by the external flow.

DOI: 10.13009/EUCASS2025-301

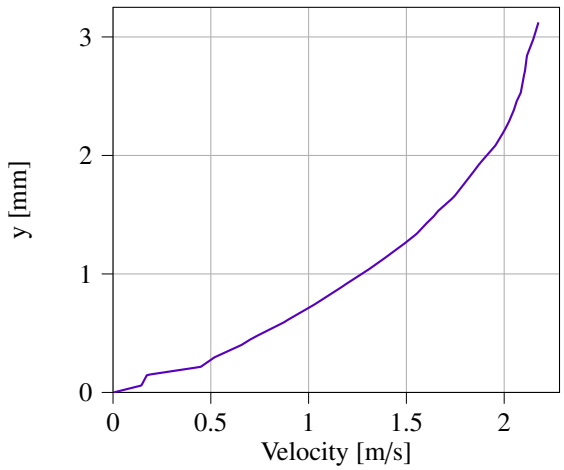

Figure 11: Boundary layer velocity profile for 25 kV at $x = 65$ mm. $y = 0$ is the approximate location of the collector surface.

8. Concluding Remarks

The present work showcases high-resolution near-wall velocity fields in the vicinity of an electroaerodynamic thruster, enabling new insights into the momentum transfer. Time-averaged velocity fields show the operating-voltage-invariant flow field topology, while instantaneous flow fields reveal the presence of significant wake instabilities and vortex shedding. The performance and stability of multi-stage thruster arrays could be impacted by fluctuating inflow conditions created by upstream thrusters. Future investigations should investigate the impact of the collector shape on wake instabilities.

Accurate thrust estimation from particle image velocimetry data was shown in the quiescent case. Crucially, the integral momentum balance must account for momentum flux fluctuations, as the momentum flux of the time-averaged velocity field underestimates the thrust measured by the load cell. While the thrust estimation was accurate across a large range of voltages, a drawback remains in the much greater standard deviation when compared to the load cell measurements. As a logical next step, the presented method can be investigated in non-zero bulk velocity.

For a rigorous optimization of EAD thrusters, the importance of quantifying drag forces was discussed. The initial attempt to estimate friction drag by analyzing the boundary layer as yet remained inconclusive. The velocity profiles in the near-wall region did not conform to classical models, suggesting complex flow phenomena such as partial detachment may be occurring. Other avenues might accordingly be explored, including direct measurement of the drag force by load cell and/or a comprehensive reevaluation of existing collector profiles so as to identify less sensitive separation properties for the given application.

9. Acknowledgments

This project has received funding from the European Union's Horizon Europe Research and Innovation Programme under grant agreement No 101098900. Views and opinions expressed are however those of the author(s) only and do not necessarily reflect those of the European Union or European Innovation Council and SMEs Executive Agency (EISMEA). Neither the European Union nor the granting authority can be held responsible for them.

Appendix: Environmental Quantities

Table 1: Environmental quantities for the experimental investigations of Section 4

Gap distance d [mm]	**Mean temperature** [°C]	**Mean relative humidity** [%]	**Mean pressure** [hPa]
20	22.5	37.5	1007.9
30	21.1	31.6	1005.3

DOI: 10.13009/EUCASS2025-301

Table 2: Environmental quantities for the experimental investigations of Section 5

Operating Voltage [kV]	**Mean temperature** [°C]	**Mean relative humidity** [%]	**Mean pressure** [hPa]
15	22.4	36.7	1002.4
20	22.4	36.3	1002.4
22.5	22.4	36.7	1002.4
25	22.4	36.7	1002.3
27.5	22.4	36.3	1002.4
30	21.2	30.4	1005.2

Table 3: Environmental quantities for the experimental investigations of Section 6

Operating Voltage [kV]	**Mean temperature** [°C]	**Mean relative humidity** [%]	**Mean pressure** [hPa]
15	23.4	61.9	1002.8
20	23.6	61.1	1002.8
22.5	23.6	60.8	1002.8
25	22.1	59.4	1002.7
27.5	23.6	61.0	1002.8
30	23.8	59.2	1002.9

References

[1] M. Belan, J. Baldo, O. Kahol, and D. Montenero. Blade emitters for atmospheric ionic thrusters. *Journal of Physics D: Applied Physics*, 57(19):195201, February 2024.

[2] M. Belan, L. Arosti, R. Polatti, F. Maggi, S. Fiorini, and F. Sottovia. A parametric study of electrodes geometries for atmospheric electrohydrodynamic propulsion. *Journal of Electrostatics*, 113:103616, September 2021.

[3] M. Belan, R. Terenzi, S. Trovato, and D. Usuelli. Effects of the emitters density on the performance of an atmospheric ionic thruster. *Journal of Electrostatics*, 120:103767, November 2022.

[4] P. Cooperman. A theory for space-charge-limited currents with application to electrical precipitation. *Transactions of the American Institute of Electrical Engineers, Part I: Communication and Electronics*, 79(1):47–50, March 1960.

[5] C. Enloe, M. McHarg, G. Font, and T. McLaughlin. Plasma-induced Force and Self-induced Drag in the Dielectric Barrier Discharge Aerodynamic Plasma Actuator. In *47th AIAA Aerospace Sciences Meeting including The New Horizons Forum and Aerospace Exposition*, Aerospace Sciences Meetings. American Institute of Aeronautics and Astronautics, January 2009.

[6] C. K. Gilmore and S. R. H. Barrett. Electrohydrodynamic thrust density using positive corona-induced ionic winds for in-atmosphere propulsion. *Proceedings of the Royal Society A: Mathematical, Physical and Engineering Sciences*, 471(2175):20140912, March 2015.

[7] C. K. Gilmore and S. R. Barrett. Electroaerodynamic Thruster Performance as a Function of Altitude and Flight Speed. *AIAA Journal*, 56(3):1105–1117, March 2018.

[8] N. Gomez-Vega and S. R. H. Barrett. Order-of-Magnitude Improvement in Electroaerodynamic Thrust Density with Multistaged Ducted Thrusters. *AIAA Journal*, 62(4):1342–1353, April 2024.

[9] M. Hamdi, M. Havet, O. Rouaud, and D. Tarlet. Comparison of different tracers for PIV measurements in EHD airflow. *Experiments in Fluids*, 55(4):1702, March 2014.

[10] A. R. Hoskinson, N. Hershkowitz, and D. E. Ashpis. Force measurements of single and double barrier DBD plasma actuators in quiescent air. *Journal of Physics D: Applied Physics*, 41(24):245209, November 2008.

[11] O. Kahol, M. Belan, M. Pacchiani, and D. Montenero. Scaling relations for the geometry of wire-to-airfoil atmospheric ionic thrusters. *Journal of Electrostatics*, 123:103815, May 2023.

[12] V. Y. Khomich, V. E. Malanichev, and I. E. Rebrov. Electrohydrodynamic thruster for near-space applications. *Acta Astronautica*, 180:141–148, March 2021.

DOI: 10.13009/EUCASS2025-301

[13] J. Kriegseis, A. Duchmann, C. Tropea, and S. Grundmann. On the classification of dielectric barrier discharge plasma actuators: A comprehensive performance evaluation study. *Journal of Applied Physics*, 114(5):053301, August 2013.

[14] J. Kriegseis, S. Grundmann, and C. Tropea. Power consumption, discharge capacitance and light emission as measures for thrust production of dielectric barrier discharge plasma actuators. *Journal of Applied Physics*, 110(1):013305, July 2011.

[15] K. Masuyama and S. R. H. Barrett. On the performance of electrohydrodynamic propulsion. *Proceedings of the Royal Society A: Mathematical, Physical and Engineering Sciences*, 469(2154):20120623, June 2013.

[16] N. Monrolin, F. Plouraboué, and O. Praud. Electrohydrodynamic Thrust for In-Atmosphere Propulsion. *AIAA Journal*, 55(12):4296–4305, December 2017.

[17] N. Monrolin, O. Praud, and F. Plouraboué. Electrohydrodynamic ionic wind, force field, and ionic mobility in a positive dc wire-to-cylinders corona discharge in air. *Physical Review Fluids*, 3(6):063701, June 2018.

[18] C. L. Nelson and D. S. Drew. High Aspect Ratio Multi-Stage Ducted Electroaerodynamic Thrusters for Micro Air Vehicle Propulsion. *IEEE Robotics and Automation Letters*, 9(3):2702–2709, March 2024.

[19] T. B. Nickels. Inner scaling for wall-bounded flows subject to large pressure gradients. *Journal of Fluid Mechanics*, 521:217–239, December 2004.

[20] F. Picella, D. Fabre, and F. Plouraboué. Numerical Simulations of Ionic Wind Induced by Positive DC-Corona Discharges. *AIAA Journal*, 62(7):2562–2573, July 2024.

[21] M. Robinson. Movement of air in the electric wind of the corona discharge. *Transactions of the American Institute of Electrical Engineers, Part I: Communication and Electronics*, 80(2):143–150, May 1961.

[22] S. Trovato, R. Terenzi, D. Usuelli, and M. Belan. Wind tunnel testing and performance modeling of an atmospheric ion thruster. *Journal of Physics D: Applied Physics*, 58(1):015201, October 2024.

[23] D. Usuelli, R. Terenzi, S. Trovato, and M. Belan. Performance Enhancement of EAD Thrusters With Nonuniform Emitters Array. *IEEE Transactions on Plasma Science*, 52(11):5414–5421, November 2024.

[24] J. Westerweel and F. Scarano. Universal outlier detection for PIV data. *Experiments in Fluids*, 39(6):1096–1100, December 2005.

[25] J. Wilson, H. D. Perkins, and W. K. Thompson. An Investigation of Ionic Wind Propulsion. Technical Report NASA/TM-2009-215822, December 2009.

[26] H. Xu, Y. He, K. L. Strobel, C. K. Gilmore, S. P. Kelley, C. C. Hennick, T. Sebastian, M. R. Woolston, D. J. Perreault, and S. R. H. Barrett. Flight of an aeroplane with solid-state propulsion. *Nature*, 563(7732):532–535, November 2018.

[27] B. Zhang, J. He, and Y. Ji. Dependence of the average mobility of ions in air with pressure and humidity. *IEEE Transactions on Dielectrics and Electrical Insulation*, 24(2):923–929, April 2017.